Research Article | Vol. 32, No. 16 / 29 Jul 2024 / Optics Express 28215
Optics EXPRESS

Full mission evaluation of EnMAP water leaving reflectance products using three atmospheric correction processors

MARIANA A. SOPPA,[1] MAXIMILIAN BRELL,[2] SABINE CHABRILLAT,[2,3] LEONARDO M. A. ALVARADO,[1,4] PETER GEGE,[5] STEFAN PLATTNER,[5] IAN SOMLAI-SCHWEIGER,[5] THOMAS SCHROEDER,[6] FRANÇOIS STEINMETZ,[7] DANIEL SCHEFFLER,[2] VITTORIO E. BRANDO,[8] MARIANO BRESCIANI,[9] CLAUDIA GIARDINO,[9] SIMONE COLELLA,[8] DIETER VANSTEENWEGEN,[10] MAXIMILIAN LANGHEINRICH,[11] EMILIANO CARMONA,[11] MARTIN BACHMANN,[11] MIGUEL PATO,[11] SEBASTIAN FISCHER,[12] AND ASTRID BRACHER[1,13,*]

[1]*Alfred Wegener Institute Helmholtz Centre for Polar and Marine Research, 27570 Bremerhaven, Germany*
[2]*GFZ German Research Centre for Geosciences, Potsdam, Germany*
[3]*Leibniz University Hannover, Institute of Soil Science, 30419 Hannover, Germany*
[4]*Currently with German Aerospace Center (DLR), Remote Sensing Technology Institute, Weßling, Germany*
[5]*German Aerospace Center (DLR), Remote Sensing Technology Institute, Weßling, Germany*
[6]*Commonwealth Scientific and Industrial Research Organisation (CSIRO), Environment, Brisbane, Australia*
[7]*HYGEOS, Lille, France*
[8]*Consiglio Nazionale delle Ricerche, Istituto di Scienze Marine (ISMAR-CNR), Rome, Italy*
[9]*Consiglio Nazionale delle Ricerche, Istituto per il Rilevamento Elettromagnetico dell'Ambiente (IREA-CNR), Milan, Italy*
[10]*Flanders Marine Institute, Oostende, Belgium*
[11]*Earth Observation Center (EOC), German Aerospace Center (DLR), Weßling, Germany*
[12]*Space Agency, German Aerospace Center (DLR), Bonn, Germany*
[13]*Institute of Environmental Physics, University of Bremen, Otto-Hahn-Allee 1, 28359 Bremen, Germany*
[*]*astrid.bracher@awi.de*

Abstract: This study presents what we believe is the first extensive assessment of the water reflectance products from the German hyperspectral Environmental Mapping and Analysis Program (EnMAP). We evaluate EnMAP's standard normalized water leaving reflectance $[\rho_W]_N$ over 17 water sites in the first two years of the mission. The EnMAP $[\rho_W]_N$ standard product is generated by a dedicated water atmospheric correction (AC) called the Modular Inversion Program (MIP). The quality of the $[\rho_W]_N$ retrievals was assessed using *in situ* hyperspectral measurements and Aerosol Robotic Network - Ocean Colour (AERONET-OC) multispectral measurements. The results showed very good agreement between *in situ* hyperspectral match-ups and EnMAP $[\rho_W]_N$, with an underestimation of EnMAP of −17.37% (bias, β) and an error (ϵ) of 23.75% at 418 – 797 nm. Two other AC processors were also investigated: the polynomial based algorithm applied to MERIS (Polymer) and the atmospheric correction for OLI lite (Acolite). The intercomparison exercise between the three AC methods applied to EnMAP data using the hyperspectral match-up dataset showed better statistical metrics for MIP ($\epsilon = 23\%, \beta = -17.37\%$) compared to Polymer ($\epsilon = 42.20\%, \beta = -2.43\%$) and Acolite ($\epsilon = 97\%, \beta = 97\%$). The superior performance of MIP was further confirmed by the validation results obtained with the multispectral match-up dataset; MIP retrievals show good agreement with *in situ* measurements at the majority of study sites.

#523813 https://doi.org/10.1364/OE.523813

Received 18 Mar 2024; revised 5 Jun 2024; accepted 16 Jun 2024; published 22 Jul 2024

Optics EXPRESS

Conversely, Polymer and Acolite retrievals tended to overestimate, especially in clearer waters as the Lampedusa study site.

1. Introduction

Spaceborne aquatic remote sensing, also called ocean colour, began in 1978 with the launch of the multispectral Coastal Zone Color Scanner, and since then, dozens of missions have been developed with significant technological improvements [1,2]. The latest development direction taken by the ocean colour missions is the imaging spectroscopy or hyperspectral remote sensing. However, for more than three decades, hyperspectral remote sensing has been used to monitor inland and coastal waters with airborne and spaceborne hyperspectral sensors developed primarily for terrestrial applications (e.g. Hyperion [3], Compact High-Resolution Imaging Spectrometer - CHRIS [4]). The Hyperspectral Imager for the Coastal Ocean (HICO) onboard the International Space Station (ISS) was the only dedicated aquatic hyperspectral mission, acquiring data at a spectral resolution of approximately 5.7 nm and a spatial resolution of 90 m from 2009 to 2015. Its data were used for a variety of aquatic studies [5–10].

One of the main advantages of hyperspectral remote sensing is that it provides measurements over hundreds of narrow contiguous bands from the visible to the infrared, allowing existing algorithms to be better adapted and new ones to be developed to explore the subtle optical spectral differences between different water types [11]. Recognising the value of such technology, a new generation of spaceborne sensors for terrestrial and aquatic applications has been developed in recent years by national and international space agencies, apart from commercial missions. Most recently, in February 2024, the National Aeronautics and Space Administration (NASA) launched the Plankton, Aerosol, Cloud, Ocean Ecosystem (PACE, [12]) with a spatial resolution of 1 km, primarily for ocean remote sensing applications. Other hyperspectral missions, but with higher spatial resolution and therefore more suitable for studies of inland and coastal waters, include the Environmental Mapping and Analysis Program (EnMAP, [13,14]) from the German Aerospace Center (DLR) in 2022, the PRecursore IperSpettrale della Missione Applicativa (PRISMA, [15,16]) sensor from the Italian Space Agency (ASI) in 2019 and the German Aerospace Center's (DLR) Earth Sensing Imaging Spectrometer (DESIS, [17]) on board the ISS in 2018. Recent studies have shown the potential of these new sensors for aquatic applications [8,18–22]. These findings pave the the way for upcoming missions including the Italian PRISMA Second Generation in 2025, NASA's Surface Biology Geology (SBG, [23]) from 2027, and the ESA Copernicus Hyperspectral Imaging Mission for the Environment (CHIME, [24]) planned for 2028.

The continuous spectral sampling of these sensors of spectral ranges that are normally avoided by multispectral sensors enables the estimation and correction of atmospheric influences. However, AC remains a critical step in aquatic remote sensing; particularly in the visible near-infrared (VNIR) region, where atmospheric path reflectance can constitute up to 90% of the measured top-of-radiance measured by sensors [25]. Water reflectance products are the input to most water quality retrieval algorithms and to derive inherent and apparent optical properties, which thus depend on the successful removal of atmospheric and (water) surface contributions [19]. Uncertainties in water reflectance products due to insufficient AC can hinder the application of hyperspectral satellite data [8].

This study focuses on the water reflectance products from EnMAP. Since April 2022, EnMAP has provided data with a spatial resolution of 30 x 30 m and 224 spectral bands from 418 to 2445 nm. [14] confirmed the quality of the EnMAP normalised water leaving reflectance ($[\rho_W]_N$) product during the commissioning phase. Here we take a closer look at EnMAP $[\rho_W]_N$ and evaluate it against hyperspectral and multispectral data sets from over 17 water sites and two

Optics EXPRESS

years of mission. The study is divided into two main parts. In the first part, we look at the individual performance of the standard EnMAP $[\rho_W]_N$ products, evaluating all valid match-ups. In the second part, common match-ups processed with the polynomial based algorithm applied to MERIS (Polymer, [26,27]) and the Atmospheric Correction for OLI (Acolite, [19,28]) ACs are evaluated and compared to official MIPs [29–31] processing.

2. Material and methods

2.1. In situ data and study sites

The *in situ* dataset contained multi- and hyperspectral data from 17 study sites (Fig. 1 and Table 1). For these study sites, 50 time-synchronous EnMAP images were generated, which 46 images have high quality and four images from the commissioning phase are classified as "low quality" by the ground segment; three at Lucinda Jetty Coastal Observatory (LJCO) and one at Lake Constance (Table 1). These data were not removed as their uncertainties met the mission requirements. The mission requirements defined by the EnMAP ground segment limit the uncertainty (root mean square error, RMSE) outside strong atmospheric absorption regions and for aerosol optical thickness (AOT) at 550 nm < 0.4 to: <0.04 for $400\,nm<\lambda \leq 450\,nm$; <0.02 for $450\,nm<\lambda \leq 650\,nm$; <0.01 for $650\,nm<\lambda \leq 800\,nm$. For AOT at 550 nm > 0.4, the corresponding requirement increases by 0.01.

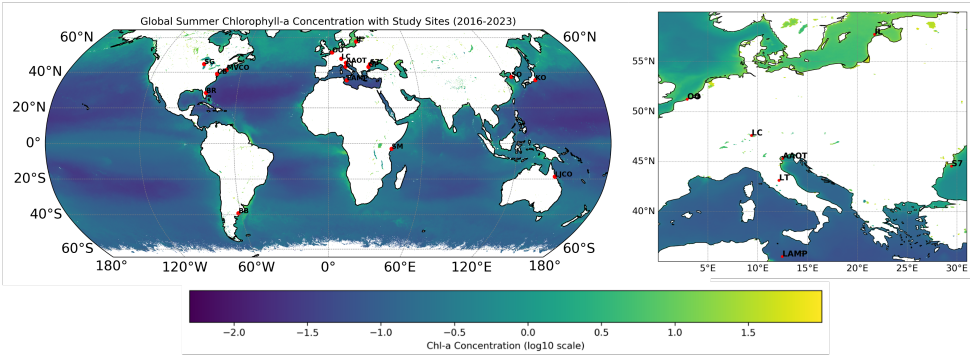

Fig. 1. Location of the validation sites over a summer climatology image of Sentinel-3A OLCI chlorophyll-a concentration [mg/m3]. Contains modified Copernicus Sentinel data processed by NASA Ocean Biology Processing Group.

Hyperpectral *in situ* measurements were collected with different instruments: PANTHYR (AAOT and Oostende), HYPERNETS (AAOT), Ocean Optics Sensor System (OOSS, Lake Constance), Sea-Bird Hyper-PRO hyperspectral radiometers (Lampedusa), WISPstation (Lake Trasimeno) and Sea-Bird hyperspectral ocean colour radiometers (HyperOCR, LJCO). Details on the measurement systems can be found in: PANTHYR [32], HYPERNETS [33], Sea-Bird Hyper-PRO [34], WISPstation [35,36], HyperOCR LJCO [37]. Nearly all measurements were collected from above-water radiometry. Data were not corrected for bidirectional effects and provided either as remote sensing reflectance (Rrs) and converted to water leaving reflectance (ρ_W) by multiplying by π, or directly as ρ_W. For Lampedusa, measurements were collected from in-water radiometry and Rrs was derived at nadir, enabling directly to convert to $[\rho_W]_N$ by multiplying by π. To avoid confusion with nomenclature we adopt the term ρ_W for the hyperspectral *in situ* measurements. Following [38,39] all hyperspectral *in situ* measurements were spectrally resampled to the spectral response function as provided in the EnMAP metadata [14].

Optics EXPRESS

Table 1. List of study sites, location, type of *in situ* measurements and number of images (C: Commissioning, O: Operational mission phase, LQ: Low Quality).

Abbreviation	Study Site	Location	*in situ* Measurement	Number of Images
AAOT	Acqua Alta Oceanographic Tower	45.31°N, 12.51°E	Hyperspectral and AERONET-OC	C: 2, O: 5
BB	Bahia Blanca	39.14°S, 61.72°W	AERONET-OC	C: 9
BR	Banana River	28.37°N, 80.63°W	AERONET-OC	O: 1
CB	Chesapeake Bay	39.12°N, 76.35°W	AERONET-OC	C: 4
GP	Galata Platform	43.04°N, 28.19°E	AERONET-OC	C: 1
IL	Irbe Lighthouse	57.75°N, 21.72°E	AERONET-OC	C: 1
KO	Kemigawa Offshore	35.61°N, 140.02°E	AERONET-OC	C: 1
LC	Lake Constance	47.63°N, 09.37°E and 47.63°N, 09.36°E	Hyperspectral	C: 1 (LQ: 1)
LT	Lake Trasimeno	43.12°N, 12.13°E	Hyperspectral	C: 1
LAMP	Lampedusa	35.49°N, 12.47°E	Hyperspectral	O: 1
LJCO	Lucinda Jetty Coastal Observatory	18.52°S, 146.39°E	Hyperspectral and AERONET-OC	C: 5 (LQ: 3), O: 10
MVCO	Martha's Vineyard Coastal Observatory	41.32°N, 70.57°W	AERONET-OC	C: 1
OO	Oostende	51.25°N, 02.92°E	Hyperspectral	O: 1
SM	San Marco	02.94°S, 40.21°E	AERONET-OC	O: 1
S7	Section-7 Platform	44.55°N, 29.45°E	AERONET-OC	C: 1
SG	South Greenbay	44.60°N, 87.95°W	AERONET-OC	C: 1
SO	Socheongcho	37.42°N, 124.74°E	AERONET-OC	C: 3

AERONET-OC measurements are collected by SeaPRISM autonomous radiometer systems [40]. AERONET-OC level 1.5 (real time cloud screened) were used for validation as coincident level 2 data with the EnMAP overpasses were not available. The AERONET-OC data were accessed at [41]. The normalized water leaving radiance data corrected for bidirectional effects based on the IOP approach [42] ($[L_W]_N IOP$) were converted to normalized water leaving reflectance $[\rho_W]_N$ by multiplying by π and dividing by the mean extraterrestrial solar irradiance [43]. For the validation we took the closest EnMAP wavelength to the original AERONET-OC bands: 444.549 and 444.699 - 443 nm, 491.633 and 491.780 - 490 nm, 510.678 and 510.829 - 510 nm, 530.268 - 532 nm, 550.525 - 551 nm, 560.947 and 561.112 - 560 nm, 622.732 and 622.921 - 620 nm, 666.435 and 666.637 - 667 nm, 679.691 - 681 nm, 706.401 - 709 nm and, 778.333 - 779 nm. The two EnMAP bands correspond to a band configuration update during the commissioning phase. For the validation of EnMAP aerosol optical thickness (AOT at 550 nm) against *in situ* AOT, we used data from the AERONET-OC sites (AOT at 551 nm or 560 nm) and one measurement from the EnMAP validation campaign at Lake Constance in 2022 during EnMAP commissioning phase using a hand-held sun photometer device Microtops II.

2.2. EnMAP data and AC processors

EnMAP Level 1B, Level 1C, and Level 2A products (processing version V010400) were obtained from the DLR Portal Earth Observation Center for the period spanning June 2022 to December 2023. Briefly, Level 1B data includes radiometric corrections and spectral characterization; Level 1C is derived from the Level 1B product and geometrically corrected (orthorectified) and re-sampled to a specified grid. Level 2A is derived from the L1C product and atmospherically

Optics EXPRESS

corrected to generate surface reflectances separately for land and water applications. More details on the EnMAP data processing levels can be found on the EnMAP website [44] and [14].

The EnMAP Level 2 $[\rho_W]_N$ product is generated by a dedicated water atmospheric correction called Modular Inversion Program (MIP) developed by EOMAP GmbH [29–31]. MIP is a physics-based AC based on multilayer atmosphere-ocean radiative transfer modelling and designed for the retrieval of water quality and bio-optical parameters from multi- and hyperspectral remote sensing measurements. MIP consists of a set of modules (e.g. modeling of atmosphere, modeling of water composition) in a continuous chain, connecting bio-physical parameters with the measured satellite top-of-atmosphere radiance [30].

We preprocessed EnMAP L1B with Polymer and EnMAP L1C data with Acolite AC to $[\rho_W]_N$ and ρ_W, respectively, to analyze and cross-compare the performances of the three processors. Polymer (v4.16.1, [26,27]) is a spectral matching algorithm in which atmospheric and oceanic signals are obtained simultaneously using the available VNIR spectrum and filtering out bands near strong atmospheric absorption features. The atmospheric reflectance, including sun glint, is modeled by a second-order polynomial, and for the water reflectance Polymer uses the bio-optical model of [45]. Details on Polymer can be found in [26,27], and the latest Polymer version is available on GitHub [46]. A first application of Polymer to simulated EnMAP data was presented in [10]. The processing of EnMAP data with Polymer has been implemented in the publicly available, alternative EnMAP Processing Tool (EnPT [47,48]) and its wrapper module ACwater [49], within the EnMAP-Box QGIS plugin [50]. The EnPT module ACwater contains all needed specifications and the technical framework required to apply the Polymer algorithm to EnMAP.

Acolite [28] is a stand-alone software based on the Dark Spectrum Fitting (DSF) algorithm in which multiple dark targets in the image are chosen to construct a dark spectrum. This representative dark spectrum is then used to estimate the atmospheric path reflectance according to the best-fitting aerosol model. Acolite can be obtained at GitHub [51], and in this study, we used the version 20231023.0 without and with the option of glint correction [19,28]. As mentioned, the Polymer algorithm is implemented in the EnPT of the EnMAP box. The EnPT processes EnMAP data from Level 1B to Level 2A, including radiometric, geometric, and atmospheric corrections (using Polymer for water surfaces) and orthorectification. In contrast, Acolite does not perform radiometric and geometric corrections, and thus its input data is Level 1C. Table 2 summarizes the main details of MIP, Polymer, and Acolite AC processors.

Table 2. Details of MIP, Polymer and Acolite AC processors.

Correction	**MIP**	**Polymer**	**Acolite**
Adjacency Effects	yes	polynomial fitting	-
Aerosol	dark pixel approach	polynomial fitting	dark target approach
Gaseous	O3	O3, NO2	O2, O3
Sun Glint	yes	yes	yes
Water Vapour	yes	-	yes
Bio-optical model	yes	yes	-
BRDF correction	yes	yes	no

2.3. Quality control

The hyperspectral validation was performed in the 420 – 800 nm spectral range, which is the range covered by all *in situ* measurements; the multispectral validation from 444 to 800 nm. As the Acolite results do not include the O2 band around 763 nm, this band was also excluded from the MIP and Polymer retrievals in the AC intercomparison exercise. As uncertainties are not provided for most of the *in situ* data, they are expected to be smaller than the mission requirements.

Optics EXPRESS

For the relative comparison between the ACs, it can be expected that all processors are affected to a similar extent by the instrument uncertainties [52]. To check for the high temporal variability of the *in situ* measurements close to the EnMAP overpass time, we calculated the mean and standard deviation at the ± 15 minute window when data were available. For three days at LJCO the *in situ* reflectance showed high temporal variability and we opted to compare EnMAP data to the mean *in situ* reflectance instead of using the closest measurement in time, as for all other *in situ* matchups.

EnMAP retrievals were compared to the *in situ* measurements following the OLCI match-up protocol [53] and using a 3 x 3-pixel box and a time window of ± 01:15. Most of the measurements were available within ± 15 minutes from the overpass (36 out of 50); 17 during the overpass. EnMAP-MIP pixels were excluded from analysis when they were masked as cirrus, cloud, cloud shadow, and haze flags. For Polymer, we found that the default flags did not always accurately correspond to invalid match-ups, so we decided not to apply any flags and investigate this issue further. For Acolite we applied the default recommended flags: NIR or SWIR threshold test, CIRRUS threshold test, TOA threshold test, NEGATIVE surface reflectance test and EXTENT test. Most of the pixels of the 3 x 3 pixel box were retained in the end, usually 7 to 9 pixels, for the valid match-ups. The EnMAP spectrum represents the median of the pixel box after the flagged and outlier pixels were removed. The number of valid match-ups of each AC processor is provided in Table 3.

Table 3. Number of valid match-ups for each AC processor (left panel) and frequency distribution (right panel) of reflectance levels the hyperspectral and multispectral *in situ* measurements (all wavelengths). *Acolite with glint correction applied.

AC Processor	Hyperspectral	Multispectral
MIP	22	24
Polymer	21	20
Acolite	11 (3*)	17 (8*)

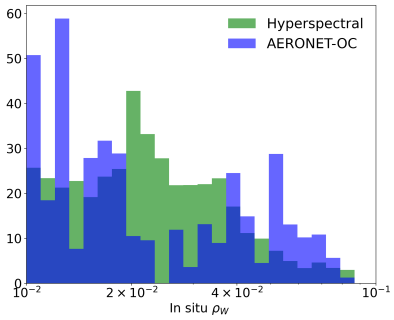

2.4. Performance metrics

Given the distribution of our match-up datasets (Table 3), we followed [52] and use two main metrics representing the overall error (ϵ, %) and bias (β, %) of the EnMAP reflectance retrievals. These metrics were calculated using log10 transformed data and then converted back to linear space [52]. We also analysed the spectral shape of EnMAP using the spectral angle mapper (SAM, θ°) to determine the similarity between an EnMAP and an *in situ* reference spectrum. The ϵ, bias β and SAM are calculated as follows:

$$\epsilon = 100 \times \text{sign}(Z) \times (10^{|Z|} - 1) \quad \text{where } Z = \text{median}\left(\log_{10}\left(\frac{y_i}{x_i}\right)\right) \tag{1}$$

$$\beta = 100 \times (10^{Y} - 1) \quad \text{where } Y = \text{median}\left|\left(\log_{10}\left(\frac{y_i}{x_i}\right)\right)\right| \tag{2}$$

$$SAM(\theta^\circ) = \frac{180}{\pi} \arccos\left(\frac{\mathbf{x_i} \cdot \mathbf{y_i}}{\|\mathbf{x_i}\|\|\mathbf{y_i}\|}\right) \tag{3}$$

Optics EXPRESS

where x indicates the measured *in situ* data and y the estimated satellite data for each match-up i.

To facilitate comparison with other studies, we also calculated the slope, intercept, and coefficient of determination (R^2) of the linear regression, the RMSE and the median absolute percentage error (MdAPE) using all values:

$$RMSE = \sqrt{\frac{1}{n}\sum_{i=1}^{n}(x_i - y_i)^2} \tag{4}$$

$$\text{MdAPE} = \text{median}\left(\frac{|y_i - x_i|}{|x_i|}\right) \times 100\% \tag{5}$$

The Pearson correlation coefficient between EnMAP-MIP $[\rho_W]_N$ ϵ and β of hyperspectral match-ups and EnMAP AOT, across off-nadir angle and solar zenith angle was used as an indicator of the relationship between EnMAP data quality and AOT, observation and illumination geometry.

3. Results and discussion

3.1. EnMAP-MIP

The assessment of EnMAP-MIP performance is illustrated in the scatterplots for match-ups to hyper- and multispectral in situ data in Fig. 2 and Table 4. A total of 22 high quality match-ups from 21 images are used for the hyperspectral validation; seven from the commissioning phase and 15 from the operational mission phase. The standard EnMAP $[\rho_W]_N$ product is highly correlated to *in situ* measurements, yet it exhibits a tendency to underestimate *in situ* ρ_W by approximately 17%, indicating an overcorrection of the atmospheric path reflectance. The overall error of about of 24% falls below the stipulated threshold of 30% uncertainty in ρ_W to ensure the data's utility as defined by the Global Climate Observing System (GCOS) for lakes [54]. The multispectral analysis confirm the findings obtained with the hyperspectral dataset, albeit with slightly improved performance metrics. It confirms, that differences between matchup products provided as $[\rho_W]_N$ or as ρ_W are marginal for our comparisons because of the strict time window for matchups and $[\rho_W]_N$ reflecting light conditions at 12:00 local time and EnMAP overpass within 24 minutes around 11:00 local time being close to this.

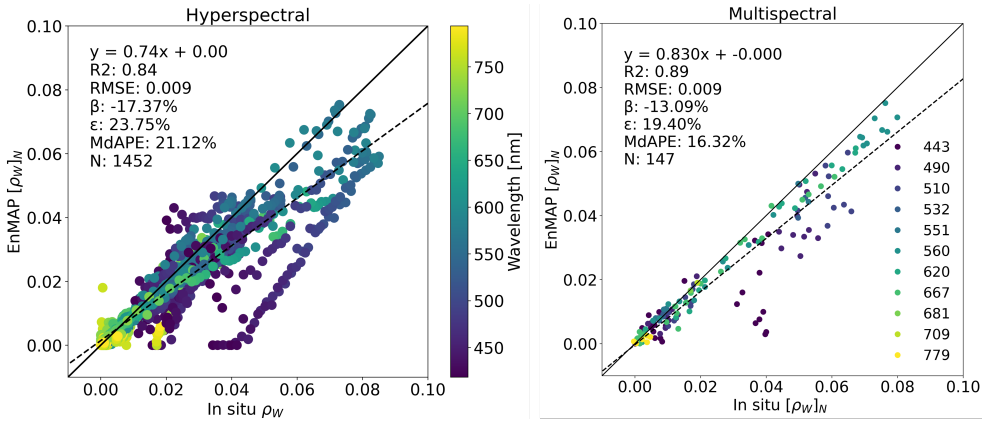

Fig. 2. Scatterplot of EnMAP-MIP $[\rho_W]_N$ for hyperspectral (N=22) and multispectral match-ups (N=24). Only valid satellite data (> 0) at the specific bands are considered in the comparison.

Optics EXPRESS

Table 4. Statistics of MIP for the two datasets: hyperspectral and multispectral (both mission phases).

Dataset	ϵ (%)	β (%)	RMSE	MdAPE (%)
Hyperspectral	23.75	−17.37	0.01	21.12
Multispectral	19.40	−13.09	0.01	16.32

Figure 3 shows the spectral comparison of EnMAP and *in situ* hyperspectral data for unique match-ups of MIP. The common match-ups between MIP, Polymer, and Acolite are provided in the next section. Overall, we observe very good agreement between EnMAP and *in situ* spectra for the different water sites and reflectance magnitudes. The highest disagreement was observed at Oostende, a region with typical turbid and very turbid waters [28]. The underestimation of MIP at Oostende might be improved by the next EnMAP processor version that should fix the issue of the different water types in the MIP processor, as now all products are retrieved using the clear water option. Three low-quality images of LJCO were acquired on dates (July 08, August 15, and August 16, 2022) when *in situ* reflectance exhibited high temporal variability (highlighted by the shaded green region). As previously mentioned, on these days, we compared the EnMAP data to the mean of the 15-minute window (indicated by the dashed green line). In the red-NIR region, there are still atmospheric absorption features that are not completely removed, in particular the O2 band around 760 nm. Overall, spectral noise, specially at shorter wavelengths, is observed in the EnMAP-MIP product and it is mostly due to an insufficient sampling in the convolution to compute water look-up-tables in MIP. This issue was recently fixed and will be present in the next EnMAP processor version. This band-to-band spectral variations are also observed in the PRISMA data by [19,22] and CHRIS-PROBA by [55], possibly a result of inter-band calibration issues.

The statistical metrics (ϵ, β, RMSE, and MdAPE) per wavelength range are illustrated in Fig. 4 and detailed in Table 5. The analysis is confined to the range up to 700 nm to avoid the NIR region having multiple atmospheric absorption features. Across the spectral range, the ϵ, RMSE, and MdAPE decline from violet-blue to red, with ϵ values between 451–700 nm meeting the 30% requirement of ρ_W for lakes. Similarly, β shows a decreasing trend towards longer wavelengths, indicating reduced overcorrection of the atmospheric effects. The uncertainty requirements set by EnMAP Ground Segment are also met. However, the strict uncertainty requirement of 5% in the blue of dedicated ocean color missions for non-optically complex waters [56] was not achieved.

Table 5. Statistics of EnMAP-MIP $[\rho_W]_N$ for two wavelength ranges (all hyperspectral match-ups).

Wavelength Range	ϵ (%)	β (%)	RMSE	MdAPE (%)
418 - 450 nm	35.08	−28.20	0.015	30.15
451 - 700 nm	19.70	−16.93	0.009	17.05

The ϵ and β of EnMAP-MIP $[\rho_W]_N$ show a significant correlation with EnMAP AOT (Fig. 5). In particular, ϵ show a positive correlation, indicating an increase in errors with higher AOT values. Conversely, β shows a negative correlation, suggesting a tendency for EnMAP $[\rho_W]_N$ to be more underestimated as AOT increases. The comparison between EnMAP AOT retrievals and *in situ* AOT measurements revealed significant uncertainties associated with EnMAP AOT. These uncertainties may have implications for the estimation of the EnMAP MIP $[\rho_W]_N$, particularly with respect to AOT values or the choice of aerosol model used in the atmospheric correction process. No relationship was found between the EnMAP-MIP $[\rho_W]_N$ quality metrics and along nadir and zenith angles.

Optics EXPRESS

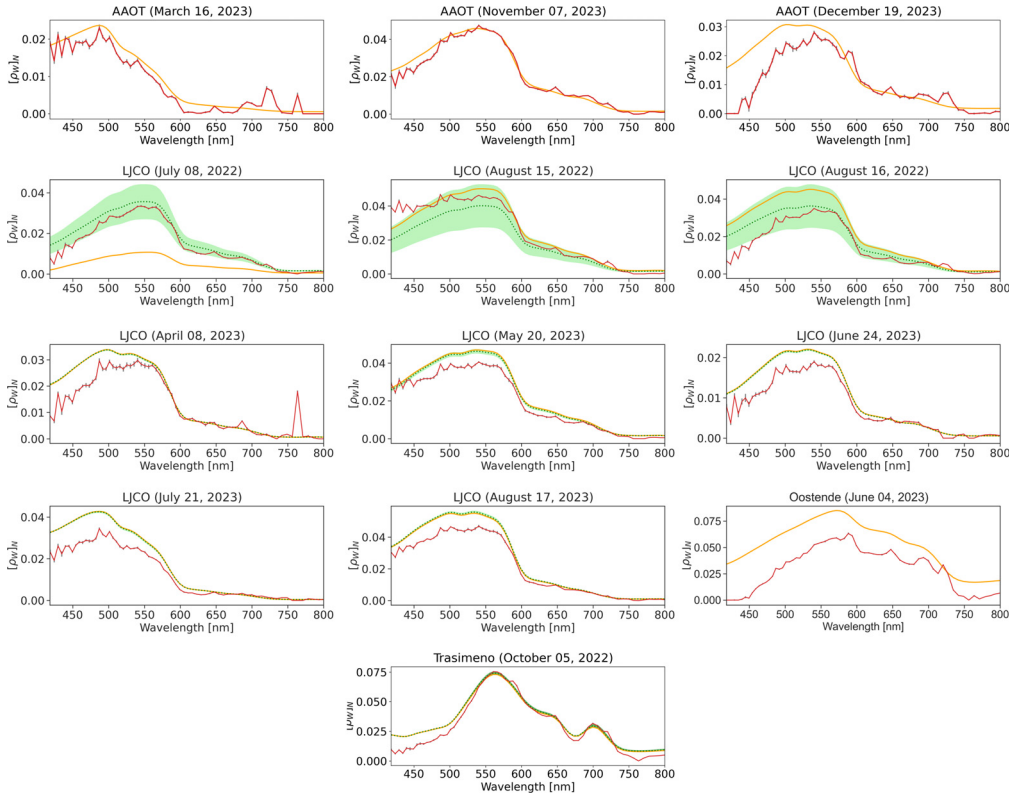

Fig. 3. Comparison of EnMAP-MIP and *in situ* hyperspectral ρ_W for selected match-ups. The median EnMAP spectra of the 3 x 3 pixel box are shown in red, with the corresponding standard deviation in grey bars (very small). The closest *in situ* measurement in time from the overpass is shown in orange, the mean and standard deviation of the ± 15 min window from the overpass in green (LJCO and Lake Trasimeno). Additional spectra are shown in Fig. 7.

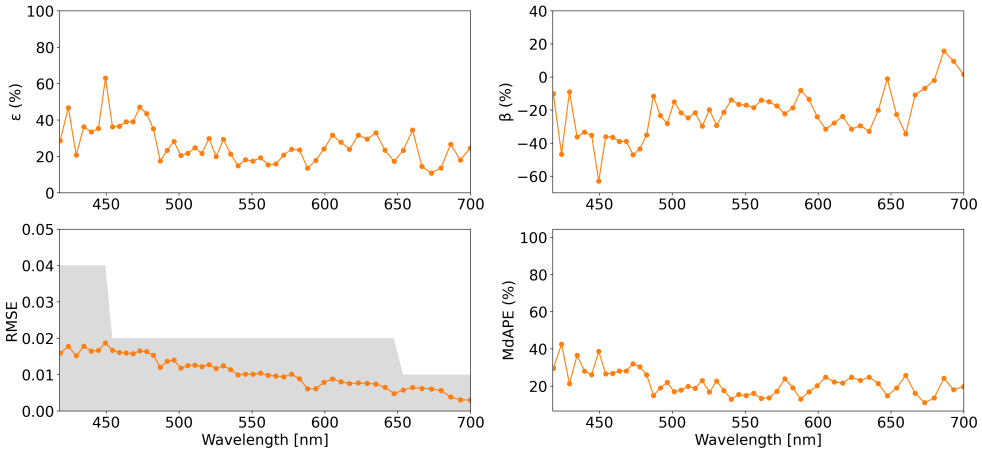

Fig. 4. Spectra of ϵ, β, RMSE and MdAPE for EnMAP-MIP $[\rho_W]_N$ for hyperspectral match-ups during the operational mission phase. The grey shaded area represents the required uncertainty (RMSE) outside of strong atmospheric absorption regions and for AOT at 550 nm lower than 0.4.

Optics EXPRESS

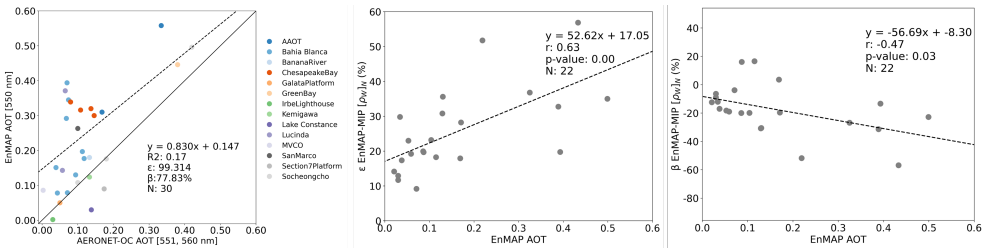

Fig. 5. Scatterplots of EnMAP AOT and *in situ* AOT (left), EnMAP-MIP $[\rho_W]_N$ overall ϵ (center) and β (right) against EnMAP AOT.

3.2. Intercomparison

Here we intercompare the performance of the three AC: MIP, Polymer and Acolite. The common hyperspectral dataset contains only 11 match-ups from four study sites (without the glint correction applied in Acolite): four at AAOT, two at Lake Constance, one at Lampedusa and four at LJCO. The selection is slightly biased to the more clear waters. The common multispectral dataset contains 14 match-ups from nine study sites: one at AAOT, four at Bahia Blanca, one at Banana River, two at Cheasepeake Bay, one at Kemigawa Offshore, one at San Marco Platform, one at Socheongcho, one at South Greenbay and two at LJCO. A summary of processors performances is illustrated in Fig. 6 and Table 6. The MIP AC gives the best results in terms of errors, followed by Polymer and Acolite. The overall bias of Polymer is close to 0, while MIP and Acolite show a clear tendency of under- and overestimation, respectively. The scatterplots of Polymer and Acolite including all high quality match-ups for each processor can be found in the Supplement 1.

Table 6. Statistics of MIP, Polymer and Acolite for the two common datasets: hyperspectral and multispectral (both mission phases).

Dataset	AC	ϵ (%)	β (%)	RMSE	MdAPE (%)
Hyperspectral	MIP	23.03	−17.37	0.01	21.80
	Polymer	42.20	−2.43	0.01	36.12
	Acolite	97.01	97.01	0.02	123.24
Multispectral	MIP	18.83	−12.57	0.01	17.13
	Polymer	65.42	−8.91	0.02	56.22
	Acolite	76.90	76.90	0.02	64.83

A comparison of all three processors in terms of spectral similarity is presented in Fig. 7. Overall, all three ACs compare well with the *in situ* measurements. The spectral noise seen in Fig. 3 is also observed here regardless the AC applied and this issue also needs further investigation, specially for Polymer. The most similar spectral shapes are retrieved by MIP; in seven out of the nine match-ups shown here. The best agreements of MIP are found at Lake Constance, an oligo- to meso-trophic lake [57], and LJCO, located in the coastal waters of the Great Barrier Reef with high concentration of sediment and colored dissolved organic matter [58–60]. Polymer and Acolite exhibited their highest agreement at LJCO. However, they also display weaker spectral similarity in the clearer waters of AAOT and Lampedusa.

In the case of Polymer, the overestimation is concentrated in the 418 - 600 nm range. On two occasions when the *in situ* spectra at AAOT transitioned to more productive waters, the Polymer $[\rho_W]_N$ retrievals show considerable improvement, as observed at Lake Trasimeno too (Fig. 8). However, the analysis of the AERONET-OC dataset reveals that this overestimation is not restricted solely to clear waters. Multispectral match-ups of Polymer show good agreement

Optics EXPRESS

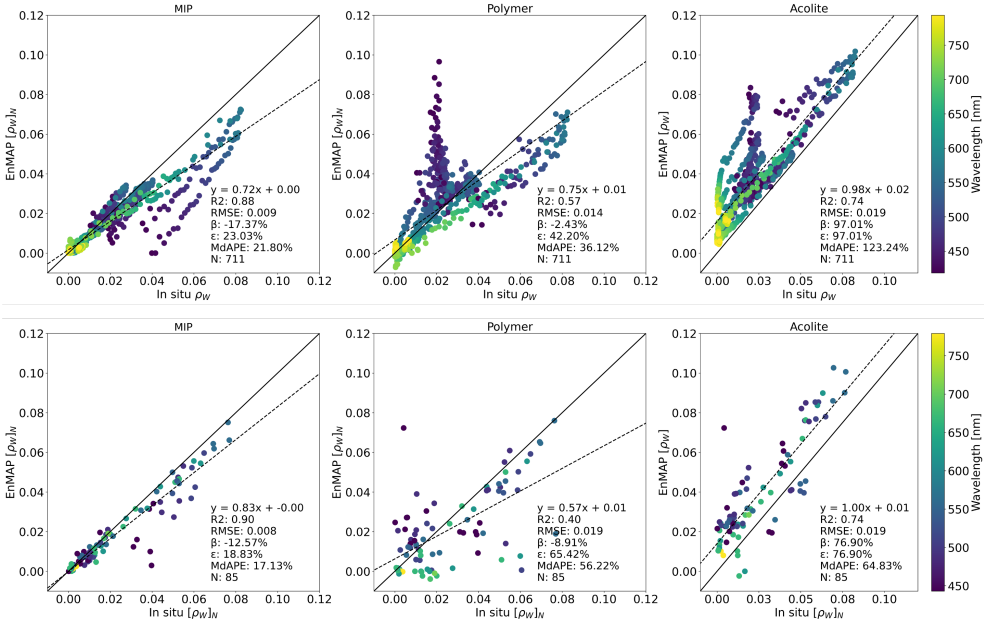

Fig. 6. Top: scatterplots of MIP, Polymer and Acolite $[\rho_W]_N$ for coincident hyperspectral match-ups (N=11). Bottom: scatterplots of MIP, Polymer and Acolite for coincident $[\rho_W]_N$ multispectral match-ups (N=14). Only valid satellite data (> 0) at the specific bands are considered in the comparison. Additional scatterplots of Polymer and Acolite (with and without glint correction) with all valid match-ups for each processor can be found in the Supplement 1.

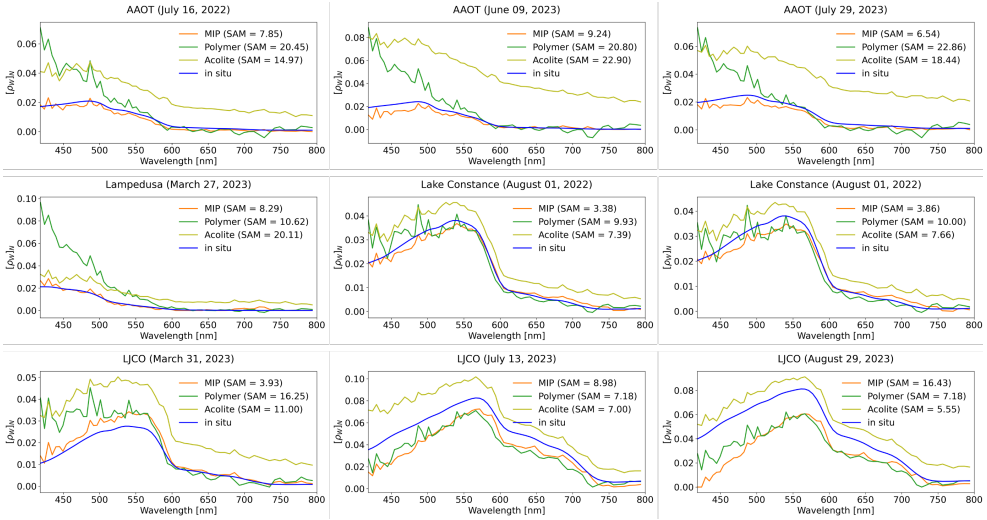

Fig. 7. Comparison between $[\rho_W]_N$ of MIP (orange), Polymer (dark green) and Acolite (light green) and *in situ* (blue). The lower the SAM value, stronger is the spectral similarity between *in situ* and satellite retrieved $[\rho_W]_N$.

Optics EXPRESS

in turbid waters, such as at Bahia Blanca, but inferior performance at sites like Socheongcho, characterized by clearer waters. These results are consistent with the match-up comparisons from the hyperspectral dataset. Nevertheless, the retrievals of Polymer in inland and coastal sites such as Banana River, Chesapeake Bay, and Green Bay also show inferior performance. One reason for the poorer results may be our decision not to use any flag information provided by Polymer. A closer examination of the bitmask information show instances where the same flag "6144" (indicating inconsistent results and excessive differences at 412 nm between retrieved and modeled water reflectance) correctly identified a bad match-up as at the Lampedusa site but erroneously flagged reliable match-ups at LJCO or Lake Trasimeno. Employing these flags would have limited our analysis to only a few match-ups.

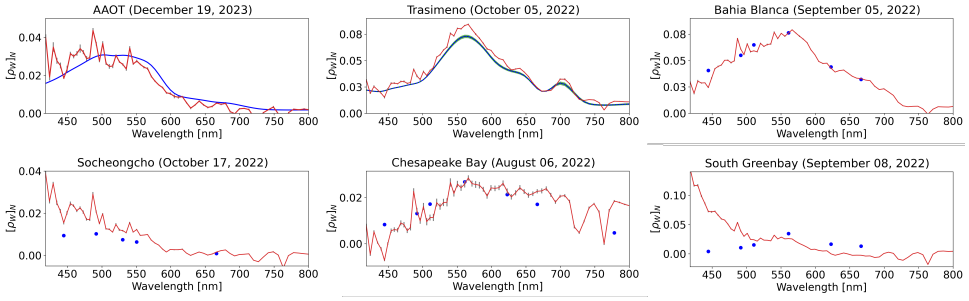

Fig. 8. Comparison of EnMAP-Polymer $[\rho_W]_N$ (red) and *in situ* ρ_W (blue) for selected match-ups.

Overall, Acolite shows an overestimation along the spectrum, probably resulting from residual sun glint or the inaccurate estimation of the aerosol model used in the AC as observed by [19] in their study of AAOT Acolite applied to PRISMA data. We also tested Acolite with the glint correction applied; it reduced the number of high quality hyperspectral match-ups from 11 to three match-ups (two at AAOT and one at Oostende). Considering the common hyperspectral match-ups, this number reduced from 11 to two match-ups only (two at AAOT). Applying the glint correction indeed improves the overestimation (see Supplement 1), as reported by [19] for PRISMA and by [61] for S2-MSI, but also flagged out reliable match-ups as at Lake Constance, LJCO, and Bahia Blanca (Fig. 9). Acolite is recognized to work especially well in productive waters and turbid where it is the main intended use [28,61], as confirmed by our results.

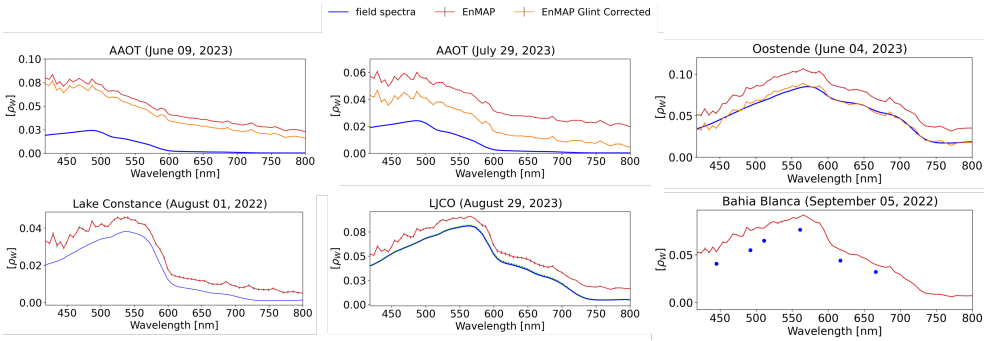

Fig. 9. Comparison of EnMAP-Acolite $[\rho_W]$ and *in situ* ρ_W (blue) for selected match-ups. Top: with (orange) and without glint (red) correction. Bottom: without glint correction

Although for MIP there have been several updates to the processor since the commissioning phase, in the case of Polymer and Acolite this study shows their first application to EnMAP data.

Optics EXPRESS

To clarify the differences between these processors, more tests are need including performance testing and optimisation of settings which was not done here and it is a limitation of our study. For example, it should be investigated whether excluding the blue spectral region (410-440 nm) from Polymer's spectral bands could improve the observed overestimation. In the case of Acolite we used all the default flags, but avoiding the use of some flags may provide useful information about the processor or sensor. For example, most of the flagged pixels in Acolite were due to negative reflectance, and avoiding this flag when processing the images would have shown in which part of the wavelength spectrum these negative values occur.

The spectra of ϵ, β, RMSE and MdAPE for common hyperspectral match-ups to all the AC results show largest uncertainties associated with wavelengths < 450 nm (Fig. 10 and Table 7) which are decreasing towards the red, except for Acolite. Also for the hyperspectral PRISMA Rrs product higher errors in the blue and in the red spectral regions was reported by [22]. The differences in β between MIP and Polymer are higher < 500 nm, improving at longer wavelengths when Polymer $[\rho_W]_N$ is about 10% underestimated, while MIP $[\rho_W]_N$ 16%. Regarding the required uncertainty as defined by EnMAP ground segment, this was only achieved by MIP water reflectance product. However, the uncertainty requirements by dedicated ocean colour missions in not-optically complex waters of 5% in the blue [56] was not achieved by any of the AC processors. Nevertheless, these waters neither fall in the mission objectives of EnMAP nor have been evaluated by the match-up results in this study.

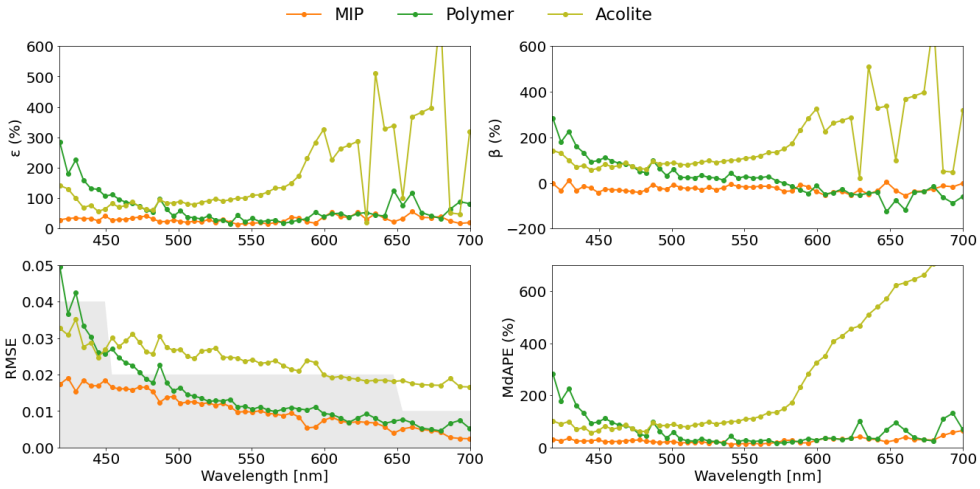

Fig. 10. Spectra of ϵ, β, RMSE and MdAPE for MIP, Polymer and Acolite for coincident hyperspectral match-ups during the operational mission phase (N=7). The grey shaded area represents the required uncertainty (RMSE) outside of strong atmospheric absorption regions as defined by the EnMAP Ground Segment and for AOT at 550 nm lower than 0.4.

Optics EXPRESS

Table 7. Statistics of MIP, Polymer and Acolite for two wavelength ranges using the common hyperspectral dataset (both mission phases).

Wavelength Range	AC	ϵ (%)	β (%)	RMSE	MdAPE (%)
418 - 450 nm	MIP	26.87	−15.84	0.01	21.99
	Polymer	118.78	105.24	0.03	97.97
	Acolite	68.85	68.85	0.02	67.23
451 - 700 nm	MIP	19.68	−17.01	0.01	18.45
	Polymer	37.45	−9.53	0.01	30.35
	Acolite	79.34	79.34	0.02	87.56

4. Conclusion

This study assessed for the first time the quality of EnMAP $[\rho_W]_N$ products. A total of 50 cloud-free EnMAP images acquired between June 2022 and December 2023 at 17 sites encompassing inland, coastal, and open ocean waters were used. Near coincident hyperspectral and multispectral measurements were also integrated into the investigation. Three AC processors have been evaluated: the standard EnMAP AC processor MIP, Polymer and Acolite. The results confirm that the EnMAP Level 1 product is accurately corrected for atmospheric and surface effects to retrieve the surface reflectance information over different water sites. The best results were obtained for the MIP AC and demonstrated the robustness of the standard EnMAP $[\rho_W]_N$ products. Polymer shows a significant overestimation for wavelengths < 600 nm, while Acolite shows an overall overestimation of the reflectance spectrum, with improved results when the glint correction is applied. Spectral noise was observed in the all three reflectance products regardless of the atmospheric correction method applied at our study sites. A larger match-up dataset in near-future will allow this study to be extended and the performance of EnMAP $[\rho_W]_N$ to be characterised by different optical water types. Further evaluation, might also benefit cross-comparing the EnMAP reflectance products to other satellite missions such as DESIS, PRISMA, and S2-MSI. The *in situ* data from various projects and study sites equipped with autonomous hyper- and multispectral radiometers played a crucial role in this study. Funding agencies are encouraged to continue supporting the advancement of this technology and the expansion of the instrument network, taking into consideration the dynamic characteristics of most aquatic ecosystems and the upcoming hyperspectral missions. Ultimately, thís study confirms the great potential of EnMAP hyperspectral data for aquatic studies and improving the knowledge on inland and coastal waters.

Funding. Bundesministerium für Wirtschaft und Klimaschutz (50EE1915, 50EE1923, 50EE2401); Agenzia Spaziale Italiana (20195HH0, 2022-15-U.0); European Space Agency (4000139081/22/I-EF, HYPERNETS-POP); Horizon 2020 Framework Programme of European Union (775983, HYPERNETS project).

Acknowledgments. The authors would like to thank all persons involved ion collecting and processing the *in situ* measurements. Thanks to Mara Gomes, Milad Niroumand-Jadidi, the members of the Phytooptics group and LUBW/ISF for supporting the Lake Constance EnMAP validation campaigns, the HYPERNETS H2020 project for the *in situ* hyperspectral data at AAOT and Lampedusa and all those involved and supporting the EnMAP Cal/Val Water Project. Thanks to Quinten Vanhellemont for the help with PANTHYR and ACOLITE data processing. Data were sourced from Australia's Integrated Marine Observing System (IMOS) – IMOS is enabled by the National Collaborative Research Infrastructure Strategy (NCRIS). NCRIS/IMOS and CSIRO are acknowledged for funding the Lucinda Jetty Coastal Observatory. We thank DLR for funding the EnMAP mission. The authors are grateful to all the principal investigators of the AERONET-OC sites: Barbara Bulgarelli, Hubert Loisel, Paula Pratolongo, Robert Frouin, Nima Pahlevan, Dirk Aurin, Frederic Melin, Hiroto Higa, Hui Feng, Heidi M. Sosik, Young-Je Park.

Disclosures. The authors declare no conflicts of interest.

Data availability. EnMAP and AERONET-OC data used in this paper are publicly available. Hyperspectral *in situ* measurements underlying the results presented may be obtained from the authors upon reasonable request.

Supplemental document. See Supplement 1 for supporting content.

Optics EXPRESS

References

1. C. R. McClain, "A decade of satellite ocean color observations," Annu. Rev. Mar. Sci. **1**(1), 19–42 (2009).
2. S. Groom, S. Sathyendranath, Y. Ban, *et al.*, "Satellite ocean colour: current status and future perspective," Front. Mar. Sci. **6**, 485 (2019).
3. V. E. Brando and A. G. Dekker, "Satellite hyperspectral remote sensing for estimating estuarine and coastal water quality," IEEE Trans. Geosci. Remote Sensing **41**(6), 1378–1387 (2003).
4. H. Lavigne, Q. Vanhellemont, K. Ruddick, *et al.*, "New processor and reference dataset for hyperspectral chris-proba images over coastal and inland waters," in *2021 IEEE International Geoscience and Remote Sensing Symposium IGARSS*, (IEEE, 2021), pp. 7916–7919.
5. W. J. Moses, A. A. Gitelson, S. Berdnikov, *et al.*, "Hico-based nir–red models for estimating chlorophyll-*a* concentration in productive coastal waters," IEEE Geosci. Remote Sensing Lett. **11**(6), 1111–1115 (2014).
6. D. J. Keith, B. A. Schaeffer, R. S. Lunetta, *et al.*, "Remote sensing of selected water-quality indicators with the hyperspectral imager for the coastal ocean (hico) sensor," Int. J. Remote. Sens. **35**(9), 2927–2962 (2014).
7. F. Braga, C. Giardino, C. Bassani, *et al.*, "Assessing water quality in the northern adriatic sea from hico™ data," Remote Sens. Lett. **4**(10), 1028–1037 (2013).
8. R. E. O'Shea, N. Pahlevan, B. Smith, *et al.*, "Advancing cyanobacteria biomass estimation from hyperspectral observations: Demonstrations with hico and prisma imagery," Remote. Sens. Environ. **266**, 112693 (2021).
9. N. Pahlevan, B. Smith, C. Binding, *et al.*, "Hyperspectral retrievals of phytoplankton absorption and chlorophyll-a in inland and nearshore coastal waters," Remote. Sens. Environ. **253**, 112200 (2021).
10. M. A. Soppa, B. Silva, F. Steinmetz, *et al.*, "Assessment of polymer atmospheric correction algorithm for hyperspectral remote sensing imagery over coastal waters," Sensors **21**(12), 4125 (2021).
11. C. Giardino, V. Brando, P. Gege, *et al.*, "Imaging spectrometry of inland and coastal waters: state of the art, achievements and perspectives," Surv. Geophys. **40**(3), 401–429 (2019).
12. P. J. Werdell, M. J. Behrenfeld, P. S. Bontempi, *et al.*, "The plankton, aerosol, cloud, ocean ecosystem mission: status, science, advances," Bull. Am. Meteorol. Soc. **100**(9), 1775–1794 (2019).
13. L. Guanter, H. Kaufmann, K. Segl, *et al.*, "The enmap spaceborne imaging spectroscopy mission for earth observation," Remote Sens. **7**(7), 8830–8857 (2015).
14. T. Storch, H.-P. Honold, S. Chabrillat, *et al.*, "The enmap imaging spectroscopy mission towards operations," Remote. Sens. Environ. **294**, 113632 (2023).
15. R. Loizzo, R. Guarini, F. Longo, *et al.*, "Prisma: The italian hyperspectral mission," in *IGARSS 2018-2018 IEEE International Geoscience and Remote Sensing Symposium*, (IEEE, 2018), pp. 175–178.
16. C. Giardino, M. Bresciani, F. Braga, *et al.*, "First evaluation of prisma level 1 data for water applications," Sensors **20**(16), 4553 (2020).
17. K. Alonso, M. Bachmann, K. Burch, *et al.*, "Data products, quality and validation of the dlr earth sensing imaging spectrometer (desis)," Sensors **19**(20), 4471 (2019).
18. M. Niroumand-Jadidi, F. Bovolo, and L. Bruzzone, "Water quality retrieval from prisma hyperspectral images: First experience in a turbid lake and comparison with sentinel-2," Remote Sens. **12**(23), 3984 (2020).
19. F. Braga, A. Fabbretto, Q. Vanhellemont, *et al.*, "Assessment of prisma water reflectance using autonomous hyperspectral radiometry," ISPRS J. Photogramm. Remote. Sens. **192**, 99–114 (2022).
20. M. Bresciani, C. Giardino, A. Fabbretto, *et al.*, "Application of new hyperspectral sensors in the remote sensing of aquatic ecosystem health: Exploiting prisma and desis for four italian lakes," Resources **11**(2), 8 (2022).
21. T. M. A. d. Lima, C. Giardino, M. Bresciani, *et al.*, "Assessment of estimated phycocyanin and chlorophyll-a concentration from prisma and olci in brazilian inland waters: A comparison between semi-analytical and machine learning algorithms," Remote Sens. **15**(5), 1299 (2023).
22. A. Pellegrino, A. Fabbretto, M. Bresciani, *et al.*, "Assessing the accuracy of prisma standard reflectance products in globally distributed aquatic sites," Remote Sens. **15**(8), 2163 (2023).
23. K. Cawse-Nicholson, P. A. Townsend, D. Schimel, *et al.*, "NASA's surface biology and geology designated observable: A perspective on surface imaging algorithms," Remote. Sens. Environ. **257**, 112349 (2021).
24. L. Cenci, M. Galli, C. Santella, *et al.*, "Analyzing the impact of the different instances of the Copernicus dem dataset on the orthorectification of VHR optical data," in *IGARSS 2022-2022 IEEE International Geoscience and Remote Sensing Symposium*, (IEEE, 2022), pp. 6001–6004.
25. H. R. Gordon, "Removal of atmospheric effects from satellite imagery of the oceans," Appl. Opt. **17**(10), 1631–1636 (1978).
26. F. Steinmetz, P.-Y. Deschamps, and D. Ramon, "Atmospheric correction in presence of sun glint: application to meris," Opt. Express **19**(10), 9783–9800 (2011).
27. F. Steinmetz and D. Ramon, "Sentinel-2 msi and sentinel-3 olci consistent ocean colour products using polymer," in *Remote sensing of the open and coastal ocean and inland waters*, vol. 10778 (SPIE, 2018), pp. 46–55.
28. Q. Vanhellemont, "Daily metre-scale mapping of water turbidity using cubesat imagery," Opt. Express **27**(20), A1372–A1399 (2019).
29. V. B. Kisselev, L. Roberti, and G. Perona, "Finite-element algorithm for radiative transfer in vertically inhomogeneous media: numerical scheme and applications," Appl. Opt. **34**(36), 8460–8471 (1995).
30. V. Kiselev, B. Bulgarelli, and T. Heege, "Sensor independent adjacency correction algorithm for coastal and inland water systems," Remote. Sens. Environ. **157**, 85–95 (2015).

Optics EXPRESS

31. B. Bulgarelli, V. B. Kisselev, and L. Roberti, "Radiative transfer in the atmosphere–ocean system: the finite-element method," Appl. Opt. **38**(9), 1530–1542 (1999).
32. D. Vansteenwegen, K. Ruddick, A. Cattrijsse, *et al.*, "The pan-and-tilt hyperspectral radiometer system (panthyr) for autonomous satellite validation measurements—prototype design and testing," Remote Sens. **11**(11), 1360 (2019).
33. C. Goyens, H. Lavigne, A. Dille, *et al.*, "Using hyperspectral remote sensing to monitor water quality in drinking water reservoirs," Remote Sens. **14**(21), 5607 (2022).
34. K. A. Casey, C. S. Rousseaux, W. W. Gregg, *et al.*, "A global compilation of in situ aquatic high spectral resolution inherent and apparent optical property data for remote sensing applications," Earth Syst. Sci. Data **12**(2), 1123–1139 (2020).
35. S. Peters, M. Laanen, P. Groetsch, *et al.*, "Wispstation: A new autonomous above water radiometer system," in *Proceedings of the Ocean Optics XXIV Conference*, Dubrovnik, Croatia, (2018), pp. 7–12.
36. M. Bresciani, M. Pinardi, G. Free, *et al.*, "The use of multisource optical sensors to study phytoplankton spatio-temporal variation in a shallow turbid lake," Water **12**(1), 284 (2020).
37. IMOS AODN, "Lucinda Jetty Coastal Observatory: HyperOCR Data," https://thredds.aodn.org.au/thredds/catalog/IMOS/SRS/OC/LJCO/catalog.html. Accessed: 11 March 2024.
38. G. Zibordi, K. Voss, B. Johnson, *et al.*, "Protocols for satellite ocean color data validation: In situ optical radiometry," IOCCG Protocols Document **3**, 67 (2019).
39. G. Tilstone, G. Dall'Olmo, M. Hieronymi, *et al.*, "Field intercomparison of radiometer measurements for ocean colour validation," Remote Sens. **12**(10), 1587 (2020).
40. G. Zibordi, B. N. Holben, M. Talone, *et al.*, "Advances in the ocean color component of the aerosol robotic network (aeronet-oc)," J. Atmospheric Ocean. Technol. **38**(4), 725–746 (2021).
41. "Aeronet seaprism version 3.0 map display," https://aeronet.gsfc.nasa.gov/new_web/draw_map_display_seaprism_v3.html.
42. Z. P. Lee, K. Du, K. J. Voss, *et al.*, "An inherent-optical-property-centered approach to correct the angular effects in water-leaving radiance," Appl. Opt. **50**(19), 3155–3167 (2011).
43. G. Thuillier, M. Hersé, D. Labs, *et al.*, "The solar spectral irradiance from 200 to 2400 nm as measured by the solspec spectrometer from the atlas and eureca missions," Sol. Phys. **214**(1), 1–22 (2003).
44. Earth Observation Center EOC at DLR, "Data Access Portal", EnMAP 1.0, (2024). [accessed date]https://www.enmap.org/data_access/
45. Y.-J. Park and K. Ruddick, "Model of remote-sensing reflectance including bidirectional effects for case 1 and case 2 waters," Appl. Opt. **44**(7), 1236–1249 (2005).
46. Y. Author, "Polymer - atmospheric correction of sun-glint contaminated ocean colour observations," GitHub, (2024). [accessed date] https://github.com/hygeos/polymer.
47. "Enmap processing tool," https://enmap.git-pages.gfz-potsdam.de/GFZ_Tools_EnMAP_BOX/EnPT/doc/about.html.
48. D. Scheffler, M. Brell, N. Bohn, *et al.*, "Enpt–an alternative pre-processing chain for hyperspectral enmap data," in *IGARSS 2023-2023 IEEE International Geoscience and Remote Sensing Symposium*, (IEEE, 2023), pp. 7416–7418.
49. "Acwater gitlab repository," https://gitlab.awi.de/phytooptics/acwater.
50. B. Jakimow, A. Janz, F. Thiel, *et al.*, "Enmap-box: Imaging spectroscopy in qgis," SoftwareX **23**, 101507 (2023).
51. N. Author, "Acolite gitlab repository," GitHub, (2024). [accessed date] https://github.com/acolite/acolite.
52. N. Pahlevan, A. Mangin, S. V. Balasubramanian, *et al.*, "Acix-aqua: A global assessment of atmospheric correction methods for landsat-8 and sentinel-2 over lakes, rivers, and coastal waters," Remote. Sens. Environ. **258**, 112366 (2021).
53. EUMETSAT, "Recommendations for sentinel-3 olci ocean colour product validations in comparison with in situ measurements – matchup protocols," Tech. rep., EUMETSAT (2022).
54. GCOS, "Essential climate variables: Lakes," https://gcos.wmo.int/en/essential-climate-variables/lakes. Accessed: 23 February 2024.
55. H. Lavigne and K. Ruddick, "Inter-band calibration for hyperspectral water remote sensing: demonstration for chris-proba," in *2021 IEEE International Geoscience and Remote Sensing Symposium IGARSS*, (IEEE, 2021), pp. 7771–7774.
56. I. O. C. C. Group, "Mission requirements for future ocean-color sensors," Tech. rep., International Ocean Colour Coordinating Group, Dartmouth, NS (2012).
57. F. Murphy, K. Schmieder, L. Baastrup-Spohr, *et al.*, "Five decades of dramatic changes in submerged vegetation in lake constance," Aquat. Bot. **144**, 31–37 (2018).
58. M. Soja-Woźniak, M. Baird, T. Schroeder, *et al.*, "Particulate backscattering ratio as an indicator of changing particle composition in coastal waters: Observations from great barrier reef waters," J. Geophys. Res.: Oceans **124**(8), 5485–5502 (2019).
59. M. Devlin, T. Schroeder, L. McKinna, *et al.*, "Monitoring and mapping of flood plumes in the Great Barrier Reef based on in situ and remote sensing observations," in *Environmental Remote Sensing and Systems Analysis*, N.-B. Chang, ed. (CRC Press, Boca Raton, FL, USA, 2012), chap. 8, pp. 147–191.
60. L. Patricio-Valerio, T. Schroeder, M. Devlin, *et al.*, "Meteorological satellite observations reveal diurnal exceedance of water quality guideline thresholds in the coastal great barrier reef," Remote Sens. **15**(9), 2335 (2023).
61. D. Doxaran, B. ElKilani, A. Corizzi, *et al.*, "Validation of satellite-derived water-leaving reflectance in contrasted French coastal waters based on hypernets field measurements," Front. Remote Sens. **4**, 1290110 (2024).